

In-plane Crushing Analysis of Cellular Materials Using Vector Form Intrinsic Finite Element

T.Y. Wu¹, W.C. Tsai² and J.J. Lee²

Abstract: The crushing of cellular materials is a highly nonlinear problem, for which geometrical, material, and contact/impact must be treated in one analysis. In order to develop a framework able to solve it efficiently and accurately, in this paper procedures for in-plane crushing analysis of cellular materials using vector form intrinsic finite element (VFIFE) is performed. A beam element of VFIFE is employed to handle large rotation and large deflection in the cell walls. An elastic-plastic material model with mixed hardening rule is adopted to account for material nonlinearity. In addition, an efficient contact/impact algorithm is designed to treat the complex contact/impact encountered in crushed cellular materials. Numerical results performed reveals that the procedures proposed in this paper are sound and reliable to simulate crushing of diverse cellular materials.

Keywords: Crushing analysis, cellular material, VFIFE.

1 Introduction

Cellular materials extensively exist in diverse plants or creatures in nature, such as in wood, bone, coral, and honeycomb and so forth. With the advancement of material science and engineering, many artificial cellular materials, such as polymer, metallic, and ceramic foams, had also been successfully developed and massively produced. They not only have the advantages of light weight and impact energy absorbing, but capable of isolating heat, noise, and vibration with respect to practical engineering needs. Therefore understanding of cellular material properties and mechanical behaviors is crucial to the quality and safety control when applying those cellular materials to engineering practices. Extensive theoretical and experimental works have been conducted for cellular materials under quasi-static and dynamic loading conditions. Good summaries in these works can be found in the references

¹ Engineering Technology & Facilities Operation, Institute of Nuclear Energy Research ROC AEC, Taiwan R.O.C.

² Department of Mechanical Engineering, National Taiwan University, Taiwan R.O.C.

of Gibson and Ashby (1997); Reid, Reddy and Peng (1993).

In the past 3 decades, many research works touched cellular materials on crushing and failure characteristics using analytical or numerical tools have been published. Gibson and his co-workers [Gibson, Ashby, Schajer, and Robertson (1982); Gibson and Ashby (1982, 1997)] conducted analyses on mechanics of two- and three-dimensional cellular materials. In their elaborations, mechanical behaviors of local single cell were examined to predict the material properties in macro scale. Experiments were also conducted to verify their analysis results. It had been proven to be useful in understanding the mechanical behavior of cellular materials through studying two-dimensional cellular materials with regular and periodic microstructures. Many works have revealed that using numerical procedures to predict properties and failure responses of cellular materials under diverse loading conditions has been extensively accepted by researchers. Papka and Kyriakides (1994, 1998) investigated in-plane crushing of a honeycomb using full scale simulations via commercial finite element code. Their results demonstrate that once the key geometric, material and processing parameters are incorporated in the models, numerical simulation is able to reproduce the experimental results both qualitatively as well as quantitatively. Nearly at the same time, Silva and Gibson (1997); Guo and Gibson (1997) analyzed the effects of removed cells on the elastic and plastic behaviors of honeycombs. However, their simulation scale and depth are very finite. Hönig and Stronge (2002a, 2002b) studied in-plane dynamic crushing of honeycombs, in which crush band initiation and wave trapping of honeycomb resulting from in-plane impact are simulated via implicit and explicit finite element approaches. In their works, both beam and shell elements were employed in respective analyses. Ruan, Lu, Wang and Yu (2003) studied the in-plane dynamic behavior of honeycombs using explicit finite element code. They found the deformation modes change significantly with different values of cell wall thickness and impact velocity. In addition, three and two localized deformation modes are respectively observed in x_1 and x_2 directions. Zheng, Yu, and Li (2005) employed two irregularity-generating approaches to create irregular honeycomb models, the crushing behaviors of which were also explored using explicit finite element code. They found the deformation modes of irregular honeycomb are more complicated than those of regular honeycomb. In order to explore the dynamic response of cellular materials and to investigate the features of the crushing front, and to examine the assumptions employed in one-dimensional shock theory [Reid and Peng (1997); Tan, Reid, Harrigan, Zou, and Li (2005)], Zou, Reid, Tan, Li, and Harrigan (2009) conducted an in-plane dynamic crushing analysis of 2D hexagon-cell honeycombs using explicit finite element code. The references with finite element simulations cited above used commercial code, ABAQUS as a numerical tool. Other renowned

commercial codes also had been employed. For instance, Liu and Zhang (2009) investigated the influence of cell micro-topology on the in-plane dynamics crushing honeycombs by LS-DYNA. Nakamoto, Tadaharu, Araki (2009a, 2009b) explored the in-plane impact behavior of honeycomb structures filled with rigid inclusions. In their work, explicit finite element code, RADIOSS was employed.

The crushing of cellular materials is highly nonlinear. Namely, all the nonlinearities of geometry, material, contact/impact, and even fragmentation must be treated in one analysis. In the author's point of view, a computational framework suitable for crushing analysis of cellular material at least must have following capabilities:

- (a) The element for modeling the deformations of cell walls must be able to account for geometric nonlinearity. The internal force evaluations must be efficient and accurate.
- (b) Generalized elastic-plastic material model must be included to simulate the material nonlinearity in cell walls.
- (c) Automatic contact search algorithm is a must to treat the complex contact behavior encountered in crushed material. The search algorithm should be linear both in the senses of memory storage and CPU cost.
- (d) The numerical algorithms in (a.-c.) must be able to be parallelized easily.

The geometrically nonlinear effect mentioned in item (a) can be treated by many ways, such as the elaborations [Iura, Suetake and Atluri (2003); Cai, Paik, and Atluri (2010); Zhu, Cai, Paik and Atluri (2010); Cai, Paik, and Atluri (2009a); Cai, Paik and Atluri (2009b)] recently published. However, cumbersome matrix manipulations should be avoided because it may be detrimental to the requisitions listed in items (c) and (d).

In order to achieve the requisitions listed in items (a-d), a framework centered at vector form intrinsic finite element (VFIFE), originally proposed by Ting and his co-workers [Ting, Shi and Wang (2004a, 2004b); Shi, Wang, and Ting (2004); Ting, Wang, Wu, Wang and Chuang (2006)] and with the capabilities mentioned above, for crushing analysis of cellular materials is developed and presented in this paper. The method of VFIFE is a set of solution procedures designed based on vector mechanics. In the past decade, elements for 2D solids [Ting, Shi and Wang (2004a); Wu, Lee and Ting (2008)], 3D solids [Wu and Ting (2004)], 3D membranes [Wu, Wang, Chuang and Ting (2007); Wu and Ting (2008)], 2D beams [Ting, Shi and Wang (2004b); Wu, Wang and Wang (2006); Wu, Tsai and Lee (2009)], and 3D beams [Ting, Wang, Wu, Wang, and Chuang (2006)] had been

successfully developed. It had been proved that all the elements can pass the tests with large overall motion and large deformation or large deflection.

In this work, a beam element of VFIFE incorporated with a nonlinear material model and an efficient contact/impact procedure is used to analyze in-plane crushing of cellular materials. The remainder of this paper is organized as follows. Section 2 introduces the concept and theory of vector form intrinsic finite element. Section 3 introduces the nonlinear material model used. Section 4 introduces a contact/impact procedure. In Section 5, numerical examples are illustrated to demonstrate the performance of the framework proposed. Finally, in Section 6, conclusions are made.

2 Vector form intrinsic finite element (VFIFE)

VFIFE is a method developed following the theory of vector form analysis proposed by Ting (2008). Rather than function, point value description is used as fundamental parameter for description. The point value description is achieved by allocating mass points (particles) for structural configuration and defining path elements for particle motion. Then properly selecting and using constitutive conditions complete the formulation. The constitutive conditions linking the mass points in deformable solids or structures are primarily complemented by the generalized forces evaluated from solid or structural units (the so-called element). Along each path element, particle motion can be described by Newton's law for free particles or by prescribed path for constrained particles [Ting (2008)].

2.1 Allocation of particles

Figure 1 illustrates a frame structure whose configuration and motion are represented by positions and trajectories of a particle set. The symbol m_β denotes the mass of an arbitrary particle β . The position vector of particle m_β at initial time t_0 , and at any time t are respectively denoted by \mathbf{x}_0 and $\mathbf{x}(t)$. At time t_0 , both the initial position \mathbf{x}_0 and initial velocity \mathbf{v}_0 are given.

The determination of particle mass in VFIFE is a modeling procedure, neither the results of variational principles nor ad-hoc numerical algorithms. In this paper, the total mass and total moment inertia of mass of an arbitrary particle β is defined as

$$\begin{aligned} m_\beta &= M_\beta + \sum_{K=1}^{nc} m_{K\beta} \\ J_\beta &= J_\beta + \sum_{K=1}^{nc} J_{K\beta} \end{aligned} \quad (1)$$

where M_β and J_β are the mass and moment inertia of mass attached to particle β ;

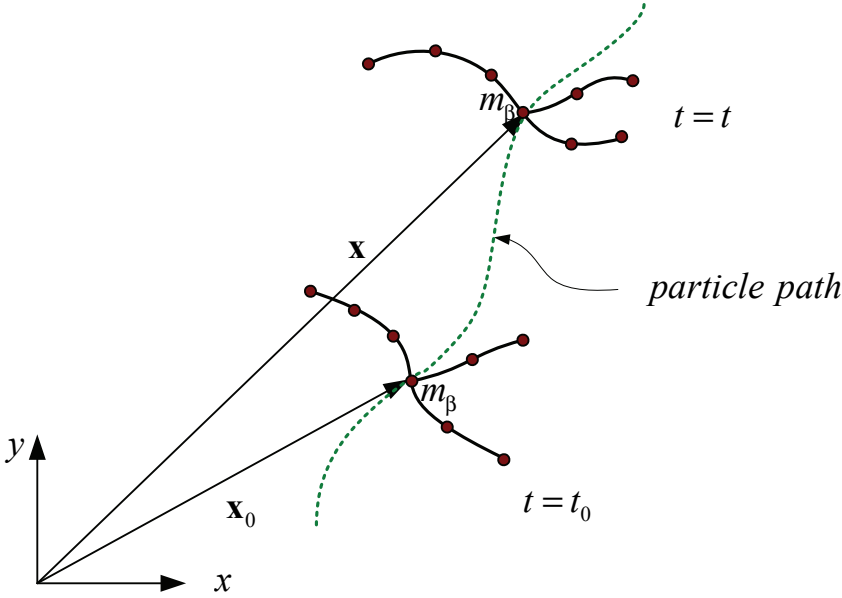


Figure 1: Point mass of structure and trajectory of a particle.

nc is the number of elements connected with particle β . $m_{K\beta}$ denotes the mass contributed from element K , which can be evaluated by

$$m_{K\beta} = \frac{1}{2} \bar{\rho}_K l_K \quad (2)$$

where $\bar{\rho}_K$ denotes the mass per unit length, and l_K the element length, of element K . $J_{K\beta}$ is the moment inertia of mass contributed from element K , which can be calculated by

$$J_{K\beta} = m_{K\beta} \gamma^2 \quad (3)$$

in which γ denotes the radius of gyration of the cross section at the node (on element K) connected to particle β . The proof of Eq. (3) can be found in the reference by Ting, Wang, Wu, Wang, and Chuang (2006).

The interaction forces between particle m_β and its neighbors are the element forces of the elements connected to the particle. The interaction forces must satisfy Newton's third law. The properties of each element are defined by nodal displacements and equivalent nodal forces. In addition, the element displacement functions must satisfy continuity conditions. Namely, the element nodal displacements are determined by particle motion and the resistant forces induced by element deformations

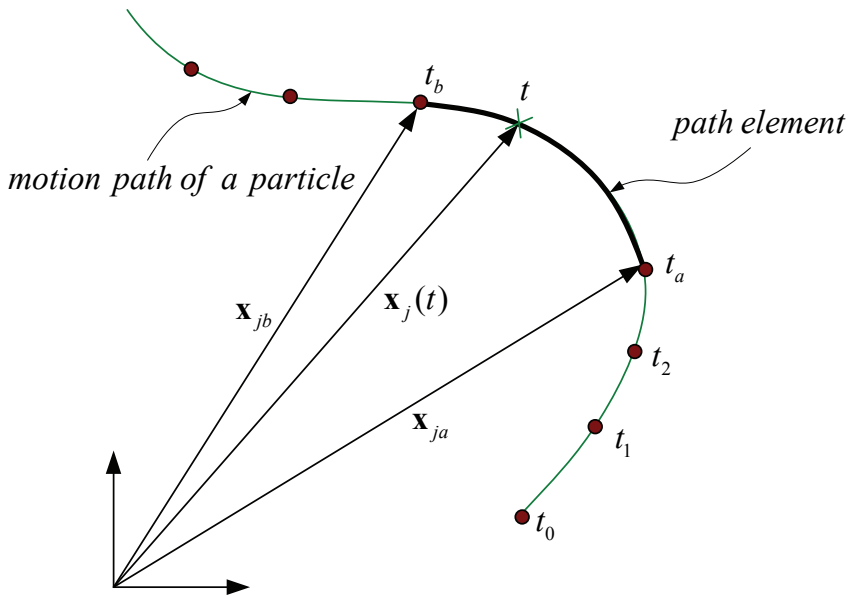


Figure 2: Particle trajectory consisted of path element.

are represented by element internal nodal forces that are applied to those particles connected with the element.

The external forces are prescribed time functions, which commonly include two types: one is the concentrated forces directly applied to particle; and the other is on the element, which must be transformed equivalently into nodal external forces.

The element doesn't carry any mass. Mass, external and internal nodal forces are lumped at particles. The planar motion of the continuum can be analyzed by Newton's law for particle motion.

2.2 Path element and governing equation

Figure 2 illustrates a particle with a motion from time t_0 to t . Its position vector continuously changes from \mathbf{x}_0 to $\mathbf{x}(t)$. Such a motion path in VFIFE is modeled via a series of consecutively jointed path elements, as illustrated in **Figure 2**. Within each path element, computational procedures are canonical and simplified. The basic assumptions for the simplified procedure are:

Assume an analysis time, say from t_0 to t_N , can be properly split into N - discrete time segments, $t_0 < t_1 < t_2 < \dots < t_a < t_b \dots < t_N$. The trajectory of particle corresponding to time $t_a \leq t \leq t_b$ is called a path element, within which the reference

configuration for stress analysis of a structural or solid unit for internal force evaluation is that at time t_a .

Within path element $t_a \leq t \leq t_b$, deformation of structural element is infinitesimal. Namely, the effect due to geometrical change within the time interval $t - t_a$ can be neglected. In each path element, standardized computation procedures including the process of displacement and deformation, the calculations for equivalent internal and external forces, and the solution of the equation of motion of each particle.

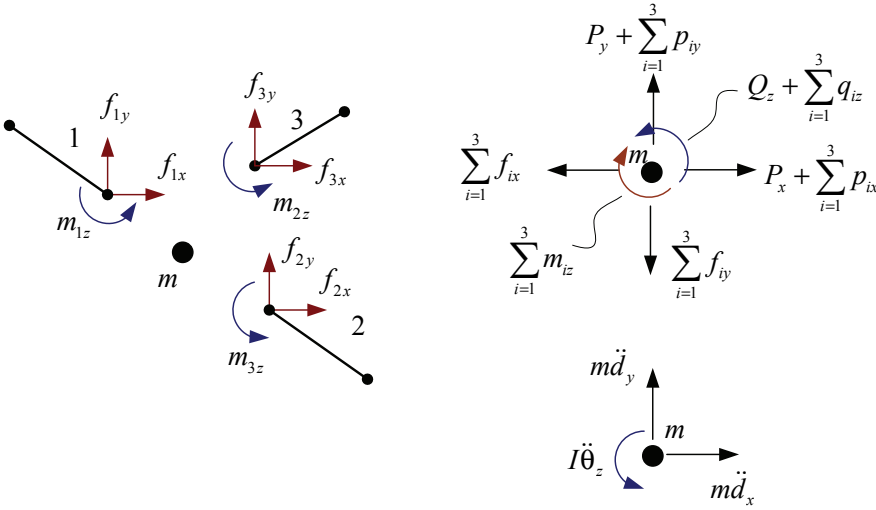


Figure 3: Free body of a particle.

Figure 3 shows a free body of an arbitrary particle with mass m . The equation of motion of particles at time t can be formulated according to Newton’s second law,

$$m\ddot{\mathbf{d}} = \mathbf{P} + \sum_{i=1}^{nc} \mathbf{p}_i - \sum_{i=1}^{nc} \mathbf{f}_i, \quad t_a \leq t \leq t_b \tag{4a}$$

or rewritten in the following explicit form,

$$\begin{bmatrix} m & 0 & 0 \\ 0 & m & 0 \\ 0 & 0 & J \end{bmatrix} \begin{bmatrix} \ddot{d}_x \\ \ddot{d}_y \\ \ddot{\theta}_z \end{bmatrix} = \begin{bmatrix} P_x \\ P_y \\ Q_z \end{bmatrix} + \sum_{i=1}^{nc} \begin{bmatrix} p_{ix} \\ p_{iy} \\ q_{iz} \end{bmatrix} - \sum_{i=1}^{nc} \begin{bmatrix} f_{ix} \\ f_{iy} \\ m_{iz} \end{bmatrix}, \quad t_a \leq t \leq t_b \tag{4b}$$

where m denotes the particle mass, and J the moment inertia of mass. d represents the particle displacement vector on plane (x, y) , including the translational

components d_x , d_y , and the rotation θ_z ; \mathbf{P} is the concentrated external force vector, including the force components P_x , P_y , and the moment Q_z , directly applied at the particle; \mathbf{p}_i is the equivalent nodal force vector, including the force p_{ix} , p_{iy} and moment component q_{iz} , contributed from the distributed loads on element i ; \mathbf{f}_i is the equivalent nodal force vector, including the force f_{ix} , f_{iy} and the moment m_{iz} , due to the deformations in element i ; nc is the number of elements connected with particle m at time t_a . The translational displacement components can be expressed as

$$\begin{bmatrix} d_x \\ d_y \end{bmatrix} = \mathbf{x}(t) - \mathbf{x}_a \quad (5)$$

where \mathbf{x}_a is the particle position vector at time t_a .

Eq. 4 needs initial conditions to get unique solution. Thus, at $t = t_a$.

$$\begin{aligned} \mathbf{d} &= \mathbf{d}_a \\ \dot{\mathbf{d}} &= \mathbf{v}_a \end{aligned} \quad (6)$$

\mathbf{v}_a denotes the particle velocity vector at time t_a .

It should be noted that both the particle mass and the number of connecting elements (nc) are kept in constant within a path element. Fragmentation of structural components or the merging of particles is only allowable at the beginning of path element, namely, t_a or t_b .

2.3 Evaluation of internal forces

In this subsection, a 2-node beam element of VFIFE for internal force evaluation is performed. **Figure 4** illustrates a planar beam element with nodal numbers (1, 2). At time t_a , the position and displacement vectors of node I are \mathbf{x}_{Ia} and \mathbf{u}_{Ia} . And, at time t they are respectively \mathbf{x}_I and \mathbf{u}_I . The displacement increment from t_a to t is

$$\Delta \mathbf{u}_I = \mathbf{x}_I - \mathbf{x}_{Ia} = \mathbf{u}_I - \mathbf{u}_{Ia}, \quad I = 1, 2 \quad (7)$$

The configuration, nodal positions, nodal internal forces and material properties of the element must be given at time t_a . Both configuration and material properties are assumed to be unchanged from time t_a to t . In other word, the material frame for internal force computation is at time t_a .

2.3.1 Reverse rigid body motion

Within path element, $t_a \leq t \leq t_b$ the material frame of the element is the configuration and position at time t_a . In this material frame, the displacement vector of

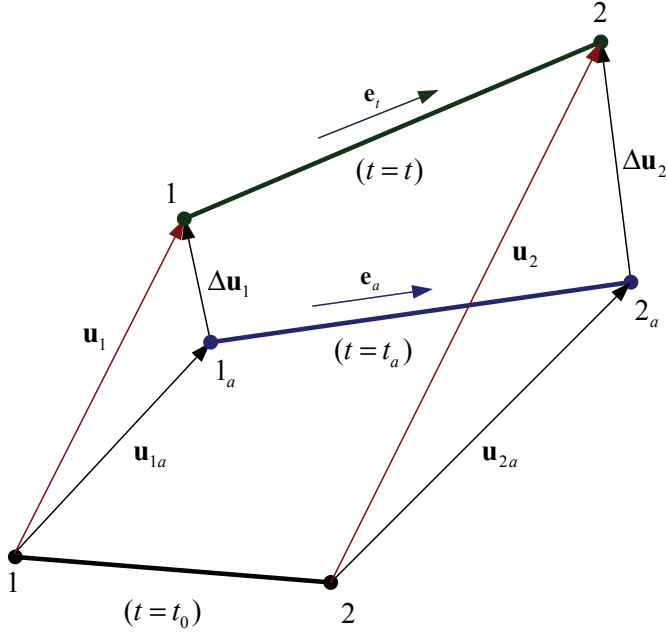


Figure 4: Nodal displacements and orientations of beam element.

an arbitrary particle is denoted by \mathbf{u}_a ; the element nodes are designated as $(1_a, 2_a)$. Let the nodal displacement increment within time segment $t - t_a$ be $\Delta\mathbf{u}_I, I=1, 2$, as illustrated in **Figure 4**. To extract pure deformation and to get consistent relationship between stress and strain, a fictitious reverse rigid body motion, including translation and rotation, is imposed on the element.

Let the element at time t undergo a fictitious reverse rigid body translation $(-\Delta\mathbf{u}_I)$, the element moves to the state with nodes designated as $(1'', 2'')$, as shown in **Figure 5**. Then, the relative nodal displacements are

$$\begin{aligned} \Delta\boldsymbol{\eta}_1 &= 0 \\ \Delta\boldsymbol{\eta}_2 &= \Delta\mathbf{u}_2 - \Delta\mathbf{u}_1 \end{aligned} \tag{8a}$$

In addition, the nodal rotation angles of the element within time segment $t - t_a$ are

$$\Delta\theta_{Iz} = \theta_{Iz} - \theta_{Iza}, \quad I = 1, 2 \tag{8b}$$

Then a reverse rigid body rotation is imposed and the nodal labels change to $(1', 2')$, as shown in **Figure 6**. Before imposing the reverse rotation, the angle of element

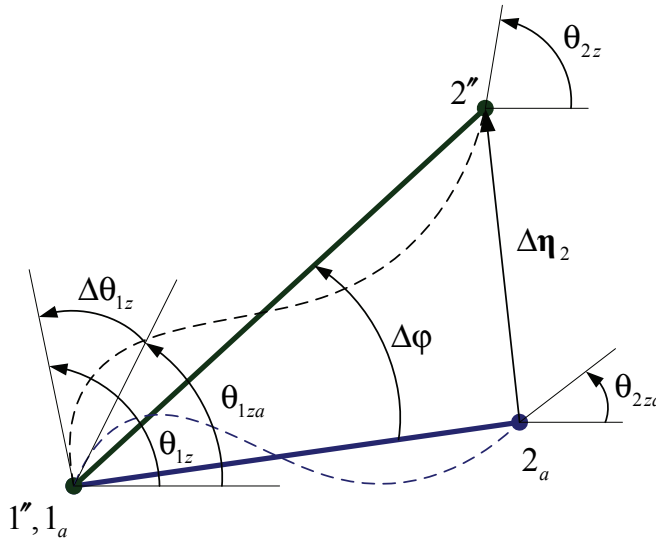


Figure 5: Nodal rotations and relative displacements.

rigid body rotation can be measured by

$$\Delta\varphi = \cos^{-1}(\mathbf{e}_a \cdot \mathbf{e}_t) \quad (9)$$

where

$$\mathbf{e}_t = \frac{\mathbf{x}_2 - \mathbf{x}_1}{\|\mathbf{x}_2 - \mathbf{x}_1\|}; \quad \mathbf{e}_a = \frac{\mathbf{x}_{2a} - \mathbf{x}_{1a}}{\|\mathbf{x}_{2a} - \mathbf{x}_{1a}\|} \quad (10)$$

represent the element orientation vectors at time t and t_a , as illustrated in **Figures 4**. Thus, the displacement due to rigid body rotation $\Delta\theta$ of each node I can be evaluated,

$$\begin{aligned} \Delta\boldsymbol{\eta}_1^r &= 0 \\ \Delta\boldsymbol{\eta}_2^r &= (\mathbf{R}^T - \mathbf{I})(\mathbf{x}_2 - \mathbf{x}_1) \end{aligned} \quad (11)$$

where \mathbf{R} is a rotation matrix, and is explicitly expressed as

$$\mathbf{R} = \begin{bmatrix} \cos(\Delta\varphi) & \sin(\Delta\varphi) \\ -\sin(\Delta\varphi) & \cos(\Delta\varphi) \end{bmatrix} \quad (12)$$

and where \mathbf{I} denotes a 2×2 identity matrix.

When the reverse motion is completed, the nodal deformation displacements can be obtained by comparing the position and configuration in the fictitious state with that in the material frame, as shown in **Figure 6**, i.e.

$$\begin{aligned} \Delta\boldsymbol{\eta}_1^d &= 0 \\ \Delta\boldsymbol{\eta}_2^d &= \Delta\boldsymbol{\eta}_2 - \Delta\boldsymbol{\eta}_2^r \end{aligned} \tag{13}$$

in which, $\Delta\boldsymbol{\eta}_I^d$ is the deformation vector of node I within the time segment $t - t_a$. In addition, the deformation nodal rotations are

$$\theta_I = \Delta\theta_{Iz} - \Delta\varphi, \quad I = 1, 2 \tag{14}$$

From **Figure 6**, one can find

$$\Delta\boldsymbol{\eta}_2^d = \Delta\mathbf{e}_a = (l - l_a)\mathbf{e}_a \tag{15}$$

where Δ is the axial stretch, l and l_a is the element length at time t and t_a .

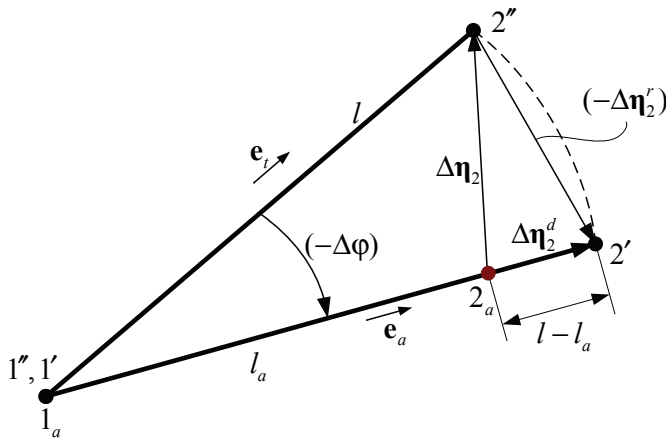


Figure 6: Reverse rotation of an element.

2.3.2 Deformation coordinate

The definition of element internal forces in VFIFE resembles that of a traditional finite element, except that the nodal variables used in VFIFE is *deformations*, rather than displacements. Therefore, three redundant DOFs' corresponding to the rigid

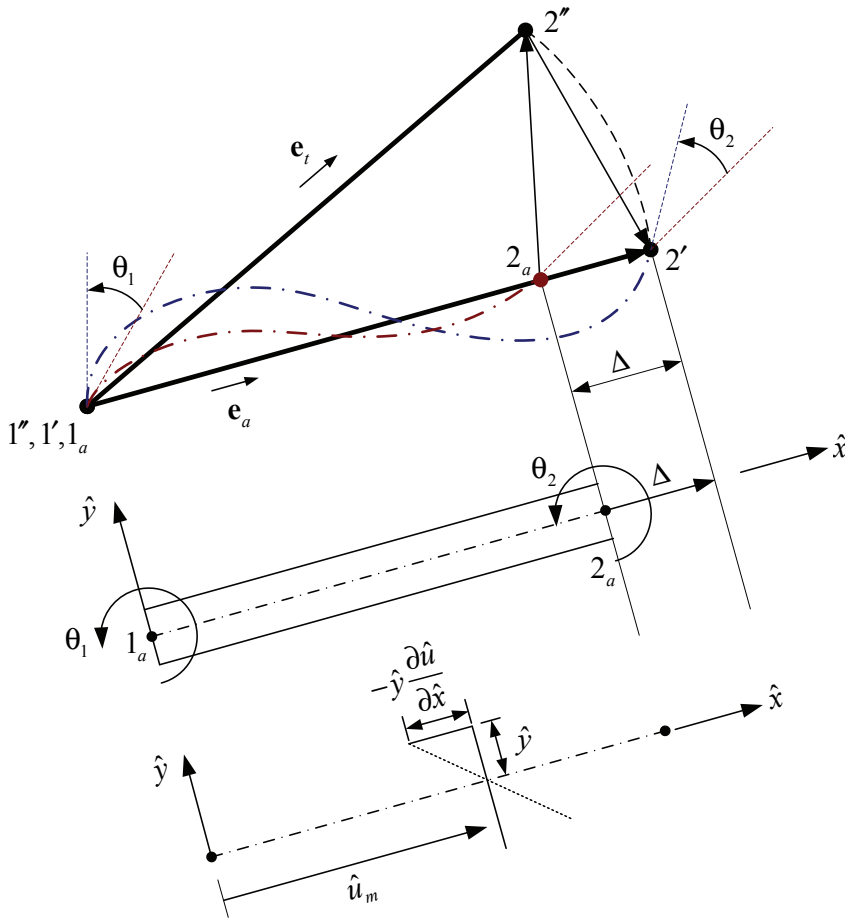


Figure 7: Deformation coordinate and Euler beam kinematics.

body modes must be eliminated. Otherwise, the variation of nodal displacements can not be arbitrary.

The elimination approach in VFIFE is defining a set of coordinate system $\hat{x} = (\hat{x}, \hat{y})$, referred to as *deformation coordinate*, for describing shape functions, as shown in **Figure 7**. Thus, a set of rectangular coordinates (\hat{x}, \hat{y}) is defined, with \hat{x} -axis parallel to the orientation vector, \mathbf{e}_a and the origin at node 1. The orientation vectors of the coordinates are

$$\hat{\mathbf{e}}_1 = \mathbf{e}_a = \begin{bmatrix} l_1 \\ m_1 \end{bmatrix}, \quad \hat{\mathbf{e}}_2 = \begin{bmatrix} -m_1 \\ l_1 \end{bmatrix} \quad (16)$$

Thus the transformation matrix from global to deformation coordinate is

$$\mathbf{Q} = \begin{bmatrix} \hat{\mathbf{e}}_1^T \\ \hat{\mathbf{e}}_2^T \end{bmatrix} = \begin{bmatrix} l_1 & m_1 \\ -m_1 & l_1 \end{bmatrix} \quad (17)$$

The relationship between deformation coordinate \hat{x} and global coordinate \mathbf{x} can be written as

$$\hat{\mathbf{x}} = \mathbf{Q}(\mathbf{x} - \mathbf{x}_1) \quad (18)$$

In what follows, any variable with a hat, e.g., $\hat{\boldsymbol{\lambda}}$, denotes that $\boldsymbol{\lambda}$ is described by a deformation coordinate, i.e., $\hat{\boldsymbol{\lambda}} = \mathbf{Q}\boldsymbol{\lambda}$.

2.3.3 Internal nodal forces

Let $\hat{\mathbf{u}}(\hat{u}, \hat{v})$ be the deformation vector of a point along the neutral axis \hat{x} , according to the Euler beam theory,

$$\hat{u} = \hat{u}_m - \hat{y} \frac{d\hat{v}}{d\hat{x}} \quad (19)$$

where \hat{u}_m is the deformation along the neutral axis (see **Figure 7**). In deformation coordinate, it satisfies

$$\text{at } \hat{x} = 0, \quad \hat{u}_m = 0, \quad \hat{v} = 0 \quad (20a)$$

$$\text{at } \hat{x} = l_a, \quad \hat{u}_m = \Delta, \quad \hat{v} = 0 \quad (20b)$$

The compatibility conditions at the nodes for deformation are

$$\text{at } \hat{x} = 0, \quad d\hat{v}/d\hat{x} = \theta_1 \quad (21a)$$

$$\text{at } \hat{x} = l_a, \quad d\hat{v}/d\hat{x} = \theta_2, \quad \hat{u}_m = \Delta \quad (21b)$$

Two polynomial functions that satisfying the six conditions above are

$$\hat{u}_m = a_1 + a_2 \hat{x} \quad (22a)$$

$$\hat{v} = a_3 + a_4 \hat{x} + a_5 \hat{x}^2 + a_6 \hat{x}^3 \quad (22b)$$

Coefficients a_i , $i = 1 \sim 6$ can be solved by the conditions in Eq. 20-21. Thus a simple substitution yields

$$\hat{u} = s\Delta - \{(1 - 4s + 3s^2)\theta_1 + (-2s + 3s^2)\theta_2\} \hat{y} \quad (23)$$

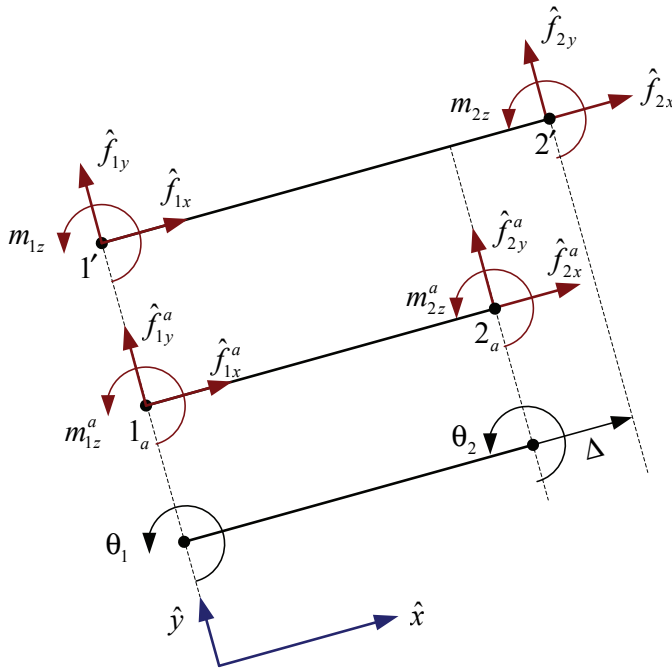


Figure 8: Element nodal forces and moments.

wheres = \hat{x}/l_a .

Assume that there is a set of nodal internal forces at nodes (1, 2), including the axial forces ($\hat{f}_{1x}, \hat{f}_{2x}$), the shear forces ($\hat{f}_{1y}, \hat{f}_{2y}$), and the moments (m_{1z}, m_{2z}), as shown in **Figure 8**. The evaluation of internal force is based on that the virtual work induced by nodal internal forces and virtual deformations must be equivalent to that by element stresses and virtual deformations. Namely,

$$\delta U_1 = \delta U_2 \tag{24}$$

in which,

$$\delta U_1 = \int_{V_a} \delta(\Delta \hat{\boldsymbol{\epsilon}})^T \hat{\boldsymbol{\sigma}} dV_a \tag{25a}$$

$$\delta U_2 = \delta(\hat{\mathbf{u}}^*) \hat{\mathbf{f}}^* = [\delta \Delta \quad \delta \theta_1 \quad \delta \theta_2] \begin{bmatrix} \hat{f}_{2x} \\ m_{1z} \\ m_{2z} \end{bmatrix} \tag{25b}$$

where, $\Delta\hat{\epsilon}$ denotes the axial fiber deformation, $\hat{\sigma}$ the total stress at an arbitrary point (\hat{x}, \hat{y}) within the element at time t , and V_a the volume of element $(1_a - 2_a)$.

The element configuration at time t_a is the material frame, deformations (\hat{u}, \hat{v}) within $t - t_a$ is small, compared to the element geometries at time t_a , such as the length l_a or cross section area A_a . Therefore, $\Delta\hat{\epsilon}$ can be defined by infinitesimal strain, i.e.,

$$\Delta\hat{\epsilon} = \frac{\partial \hat{u}}{\partial \hat{x}} = \frac{1}{l_a} \frac{\partial \hat{u}}{\partial s} \tag{26}$$

Or written in the matrix form,

$$\Delta\hat{\epsilon} = \mathbf{B}\hat{\mathbf{u}}^* = \frac{1}{l_a} [1 \quad (4 - 6s)\hat{y} \quad (2 - 6s)\hat{y}] \begin{bmatrix} \Delta \\ \theta_1 \\ \theta_2 \end{bmatrix} \tag{27}$$

Substituting Eq. 27 into Eq. 25, and from Eq. 24, yields a set of nodal forces

$$\hat{\mathbf{f}}^* = \begin{bmatrix} \hat{f}_{2x} \\ m_{1z} \\ m_{2z} \end{bmatrix} = \int_{V_a} \mathbf{B}^T \hat{\sigma} dV_a \tag{28}$$

where $\hat{\sigma}$ is the axial stress at the fictitious state $(1' - 2')$. According to the basic assumption of mechanics of material, it can be written as

$$\hat{\sigma} = \hat{\sigma}_a + \Delta\hat{\sigma} \tag{29}$$

$\hat{\sigma}_a$ is the stress at time t_a . The difference between states $(1', 2')$ and $(1_a, 2_a)$ is small, thus the incremental stress $\Delta\hat{\sigma}$ can be defined by engineering stress.

Substituting Eq. 29 into 28, we have

$$\hat{\mathbf{f}}^* = \mathbf{f}_a^* + \Delta\hat{\mathbf{f}}^* = \int_{V_a} \mathbf{B}^T \hat{\sigma}_a dV_a + \int_{V_a} \mathbf{B}^T (\Delta\hat{\sigma}) dV_a \tag{30}$$

In the work presented, the integral in Eq. 30 is carried out using Lobatto's and Gaussian integration rule respectively through the depth and along axis of element. Because of the procedure of reverse motion, the particular stress update algorithms for satisfying the principle of objectivity are not required in VFIFE [Ting (2008)].

In Eq. 30 only yields three components of internal forces of the element are available. The other three components must be calculated using three static equilibrium conditions of element:

$$\begin{aligned} \sum F_{\hat{x}} &= 0 & \hat{f}_{1x} &= -\hat{f}_{2x} \\ \sum M_{1a} &= 0 & \hat{f}_{2y} &= -(m_{1z} + m_{2z})/l_a \\ \sum F_{\hat{y}} &= 0 & \hat{f}_{1y} &= -\hat{f}_{2y} \end{aligned} \tag{31}$$

Consequently, Newton's third law is automatically satisfied.

2.3.4 Forward motion

The internal nodal forces calculated in Eq. 30 and 31 are not consistent with the orientation of the state at time t , thus a forward motion, including a translation ($+\Delta\hat{\mathbf{u}}_1$) and a rotation ($+\Delta\varphi$), must be imposed. Therefore, internal nodal forces in global orientation are obtained as follows.

$$\begin{bmatrix} f_{Ix} \\ f_{Iy} \\ m_{Iz} \end{bmatrix} = \begin{bmatrix} \mathbf{RQ}^T & 0 \\ 0 & 1 \end{bmatrix} \begin{bmatrix} \hat{f}_{Ix} \\ \hat{f}_{Iy} \\ \hat{m}_{Iz} \end{bmatrix}, \quad I = 1, 2 \quad (32)$$

Through the formulation presented above, one can find that the evaluation of internal nodal forces in VFIFE is simple and efficient.

3 Material model

In Eq. 30, the bending stress must be calculated from a stress-strain relationship. In this section, a bilinear elastic-plastic material model for numerical implementations is used. The yielding function is written as

$$\sigma_y = \sigma_y^0 + \beta H \bar{\epsilon}_p \quad (33)$$

in which the symbols σ_y^0 , σ_y , H and $\bar{\epsilon}_p$ respectively denote initial yielding stress, subsequent yielding stress, plastic hardening modulus and effective plastic strain. The combination of isotropic and kinematic hardening can be achieved via introducing a parameter, β ($-1 < \beta \leq 1$). $\beta = 1$ and $\beta = 0$ respectively stand for isotropic and kinematic hardening rule.

An algorithm degenerated from radial return mapping [Krieg and Key (1976)] is employed herein. Let the trial stress $\hat{\sigma}^*$ be the stress in material frame plus an increment of elastic stress, i.e.

$$\hat{\sigma}^* = \hat{\sigma}_a + E_a \Delta \hat{\epsilon} \quad (34)$$

where E_a is the elastic tangent modulus at stress state $\hat{\sigma}_a$. To account for kinematic hardening, the reduced stress ξ is included as follows,

$$\xi = \hat{\sigma}^* - \alpha \quad (35)$$

where α denotes the back stress due to the movement of yielding surface. Comparing reduced stress ξ with yielding stress σ_y provided by Eq. 33, if $\xi < \sigma_y$ then

the response is elastic, otherwise it is in plastic phase and the trial stress must be modified as

$$\hat{\sigma} = \hat{\sigma}^* - \Phi \cdot \xi \quad (36)$$

where Φ is a scale factor due to radial return,

$$\Phi = E_a \cdot \dot{\xi}_p / |\dot{\xi}| \quad (37)$$

in which,

$$\dot{\xi}_p = \frac{|\dot{\xi}| - \sigma_y}{E_a + H} \quad (38)$$

is the increment of effective plastic strain. The back stress can be updated by the increment of back stress,

$$\dot{\alpha} = (1 - \beta)H\dot{\xi}_p\xi/|\dot{\xi}| \quad (39)$$

The verification and validation the plasticity algorithm incorporated with VFIFE can be found in the work by Wu, Tsai and Lee (2009).

4 Contact algorithms

The contact search algorithm in this work is designed according to a global-local search strategy [Zhong (1993)]. The global search filters out most of contact candidates impossible to come into contact. The local search algorithm is built on a ball-to-segment contact methodology. In addition, penalty approach is employed for contact force evaluation. The details are specified as follows.

4.1 Contact search algorithm

Figure 9a shows a cellular structure that simply consists of 5 cells. The cell walls are modeled by several particles linked by beam elements. To achieve the balance between accuracy and computational efficiency, ball and segment are adopted as the basic contact features in the presented crushing analysis. The center of ball coincides with position of particle, and the segment body is represented by the neutral axis of beam element with a specified thickness, as illustrated in **Figure 9b**.

The contact search implementation consists of 2 phases, i.e. the global and local search phases. In the phase of global search, a background grid is used for sorting.

The sorting of particle is carried out using the integerized particle position. For instance, for an arbitrary particle i , its integerized position is (i_x, i_y) .

$$\begin{aligned} i_x &= \text{int}(x_i/B) + 1 \\ i_y &= \text{int}(y_i/B) + 1 \end{aligned} \quad (40)$$

where B denotes of the size of the bucket in the grid, which is determined according to the size of beam element. Thus the total number of buckets is $(L_x \times L_y/B^2)$. L_x and L_y are the dimensions of the grid (see **Figure 9a**). The integerized position is also the coordinate of a bucket. Thus with the integerized position of each particle, for any segment located in a bucket, only the balls (particles) in the bucket and its neighbors are checked for local contact search, as shown in **Figure 9b**.

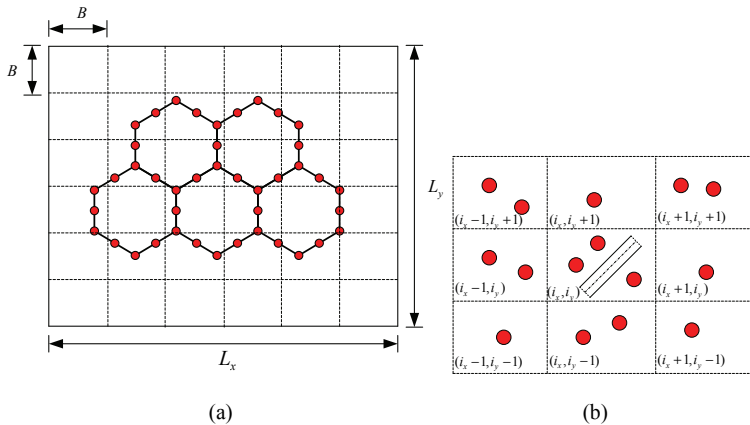


Figure 9: (a) Background grid for sorting (b) Segment body and its neighbors for contact.

The memory requirement for the storage of sorting result is commonly not linear. In this work, the NBS contact detection algorithm [Munjiza and Andrew (1998)] is adopted, rather than linked-list. The NBS algorithm was originally developed for discrete element method (DEM). It only poses the complexity of $O(N)$ both in the senses of computation speed and memory storage. In this work, only the ball-to-segment contact search is checked in analysis, i.e. the segment-to-ball contact search is neglected. Consequently, all the particles in the 9 buckets must be checked, as shown in **Figure 9b**.

Figure 10 illustrates the methodology of the local search used in this work. The basic contact features are a ball with radius R and a beam segment with a thickness

h. The contact between the ball and segment is true if and only if the following conditions are met,

$$0 \leq \mathbf{x}_{p1} \cdot \mathbf{e}_t \leq l \tag{41a}$$

$$|\mathbf{x}_{p1} - \mathbf{x}_{p1} \cdot \mathbf{e}_t| < R + h/2 \tag{41b}$$

in which, \mathbf{x}_{p1} is the relative position vector of ball *p* to node 1. \mathbf{e}_t and *l* respectively denote the orientation vector of the segment, and the segment length.

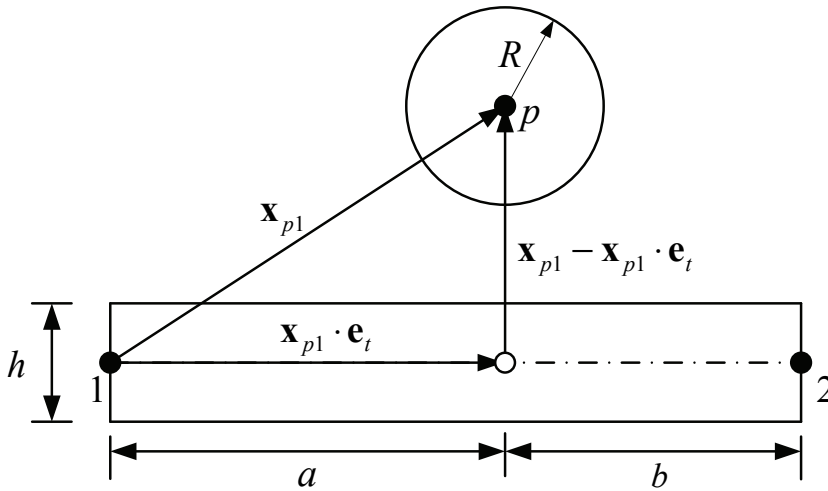


Figure 10: The ball and segment for checking local contact.

4.2 Contact force evaluation

When the ball comes into contact with the segment, a depth of penetration, D is evaluated. Namely,

$$D = |\mathbf{x}_{p1} - \mathbf{x}_{p1} \cdot \mathbf{e}_t| - (R + h/2) \leq 0 \tag{42}$$

A normal contact force is estimated using the penalty approach,

$$f_n = (k \cdot D + c \cdot \dot{D}) A_c \tag{43}$$

where c is the coefficient of viscosity, \dot{D} is the rate of penetration, and k is the penalty parameter.

The friction force is calculated using a bilinear Coulomb model. The algorithm incrementally evaluate the friction force at each new step. Let the trial frictional force be written as

$$\mathbf{f}_s^{tr} = \mathbf{f}_s^{t-\Delta t} - k\Delta\mathbf{d} \quad (44)$$

where $\mathbf{f}_s^{t-\Delta t}$ is the friction force at time $t - \Delta t$, Δd is the relative sliding displacement of ball to segment. If the magnitude of trial frictional force is less than that calculated by Coulomb's law,

$$\mathbf{f}_u = \mu |\mathbf{f}_n| \quad (45)$$

in which μ is the frictional coefficient, then the friction force at time t is the trial frictional force,

$$\mathbf{f}_s^t = \mathbf{f}_s^{tr} \quad (46)$$

Otherwise,

$$\mathbf{f}_s^t = \mathbf{f}_u \cdot \frac{\mathbf{f}_s^{tr}}{|\mathbf{f}_s^{tr}|} \quad (47)$$

5 Numerical examples

Numerical examples are performed in this section to demonstrate the proposed procedures introduced in sections 2, 3 and 4. All the numerical examples are implemented on a FORTRAN 90 code, VFIFE2D.

5.1 Example 1: Quasi-static compression of honeycomb

This example considers a honeycomb consisting of 10×15 single cells and made of AL-5052-H39 aluminum alloy, as shown in **Figure 11-12**. The honeycomb is installed between 2 plates, A and B. The plate A is fixed but plate B is slowly moved down to compress the honeycomb. The honeycomb doesn't stick to the plates. The thickness of vertical cell wall is 2 times larger than those of other 4's. In **Figure 12**, two types of single cells with distinct dimensions are analyzed. The experiments for these 2 types of honeycombs had been conducted by Papka and Kyriakides (1998).

In analysis, the material of AL-5052-H39 aluminum alloy is modeled by a bilinear elastic-plastic model with isotropic hardening rule. The material properties are also specified in **Figure 12**. A frictional coefficient of 0.2 [Papka and Kyriakides (1998)] is used to account for the frictions between plates and honeycomb. Three

particles and 2 beam elements are allocated for a single cell wall, thus totally 814 particles are used for the entire honeycomb. In each element, 2 and 6 integration points are allocated along beam axis and through sectional depth for internal force evaluation. In addition, a size of time step $\Delta t = 2.0 \times 10^{-6}$ sec is used for time integration. To achieve the quasi-static solution, the approach of dynamic relaxation is used.

Figure 13 plots the stress-strain curves from the case of *Dimensions 1*, in which the strain is the ratio of plate displacement to the original length of the honeycomb, and the stress is the averaged contact pressure acting on plate B. It can be observed that the cell wall of honeycomb starts to buckle as the strain is around 7%, then a stress plateau is developed until the strain reaching about 70 %. Over 70 % of strain, the cell walls of honeycomb holistically collapsed and contact one another, making the honeycomb densification and contact stress steeply ascending. Comparing VFIFE's result to those of 2 experiments conducted by Papka and Kyriakides (1998), the presented stress plateau is slightly larger than those from experiments, but good agreement can be observed.

Similar to the case of *Dimension 1*, Papka and Kyriakides (1998) conducted the other honeycomb with cell properties, termed *Dimensions 2* in **Figure 12**. In this case, the thickness of cell wall is reduced. **Figure 14** is the results from VFIFE and experiment. As expected, the plateau stress also reduces. In this case, the result of VFIFE also shows good agreement with that of experiment.

5.2 Example 2: Dynamic crushing of cellular materials

This example analyzes dynamic crushing of three types of cellular materials, which respectively consist of 74×21 hexagonal (*Type I*), 128×32 quadratic (*Type II*), and 128×37 regular triangular (*Type III*) cells, as illustrated in **Figure 15**. The geometry and dimensions of each type of single cell and material properties are illustrated and specified in **Figure 16**. The three materials have the same length of 512 mm, width of 128 mm, and weight of 70.77 g. In addition, the same relative density of 0.1 is used according to following Eqs,

$$\frac{\rho_Q^*}{\rho} = 2 \frac{h^Q}{L^Q} \left(1 - \frac{1}{2} \frac{h^Q}{L^Q} \right) \text{ for quadratic cell} \tag{48}$$

$$\frac{\rho_T^*}{\rho} = 2\sqrt{3} \frac{h^T}{L^T} \left(1 - \frac{\sqrt{3}}{2} \frac{h^T}{L^T} \right) \text{ for triangular cell} \tag{49}$$

$$\frac{\rho_H^*}{\rho} = \frac{\sqrt{3}}{2} \frac{h^H}{L^H} \text{ for hexagonal cell} \tag{50}$$

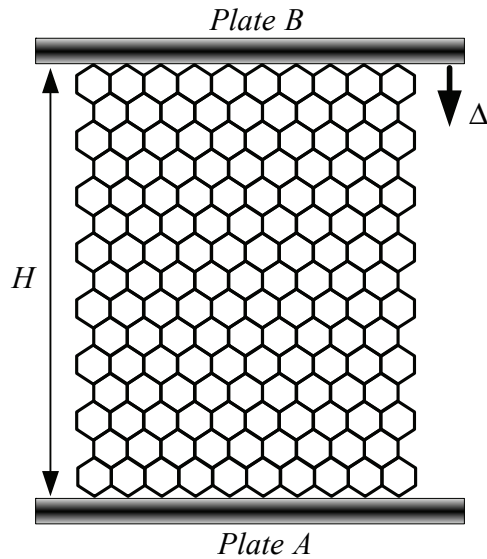
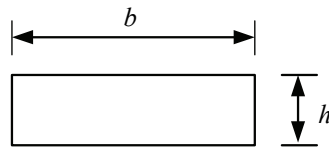
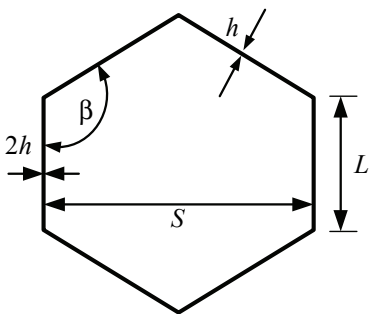


Figure 11: The honeycomb for in-plane compression test.



Material properties

Mass density: $\rho = 2.7 \times 10^{-9}$ (ton/mm³)
 Yang's modulus: $E = 69.0$ (GPa)
 Initial yielding stress: $\sigma_y^0 = 292$ (MPa)
 Tangent modulus: $E_T = 0.69$ (GPa)

<i>Dimensions 1:</i>	<i>Dimensions 2:</i>
$S = 9.5436$ mm	$S = 9.51$ mm
$L = 5.51$ mm	$L = 5.49$ mm
$\beta = 120^\circ$	$\beta = 120^\circ$
$h = 0.1448$ mm	$h = 0.1194$ mm
$b = 1.0$ mm	$b = 1.0$ mm

Figure 12: Dimensions and material properties of a single cell in **Figure 11**.

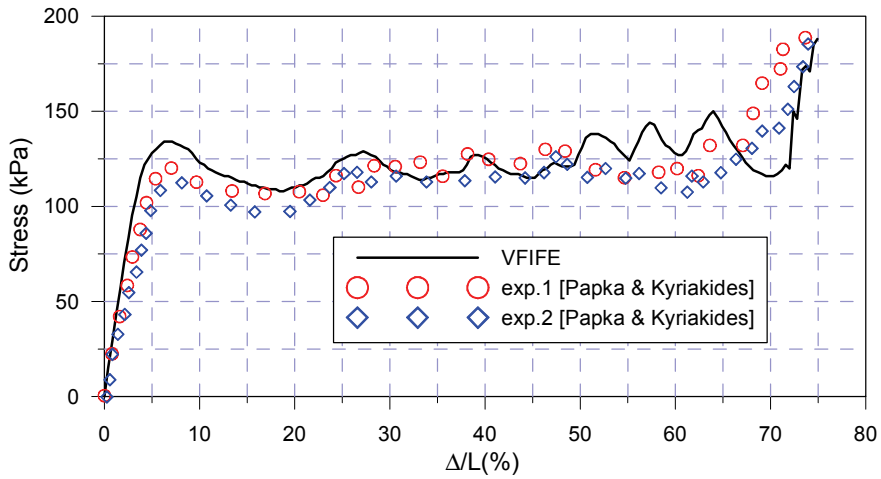


Figure 13: Stress-strain curves from the case of *Dimensions 1*.

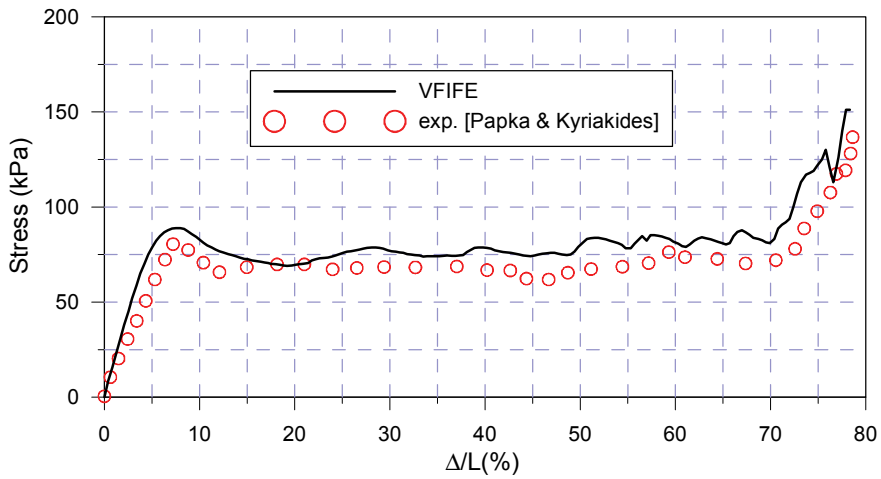


Figure 14: Stress-strain curves from the case of *Dimensions 2*.

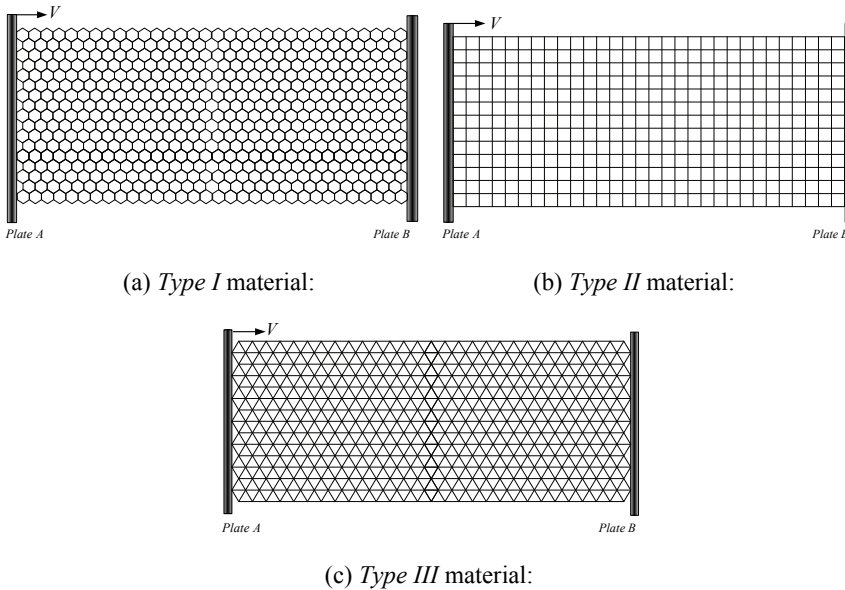


Figure 15: Three types of cellular materials compressed by a plate with velocity V .

Each single cell wall is modeled by three particles and 2 beam elements. Thus totally 8099, 4125, and 6364 particles are respectively required for the entire structure of *Type I*, *II*, and *III*. In each element, 2 and 6 integration points are respectively allocated along beam axis and through section depth to evaluate internal forces. In addition, a size of time step $\Delta t = 2 \times 10^{-7}$ sec is used for time integration.

The material model of cell wall is elastic-perfect-plastic. The contact interfaces between cell walls are assumed to be frictionless. In addition, the adherence on the interfaces between cellular material and plate is neglected. In dynamic crushing tests, the plate *B* is fixed but the plate *A* is imposed by a prescribed moving velocity, V . In this example, the materials under velocities, 2, 10, 25, 50, 75, 100, 150, and 200 m/sec are respectively examined.

Figure 17 plots the deformation process of *Type I* (hexagon) material under compression velocities, 2, 10, 50, and 100 m/sec, respectively. In the cases under slower velocities, 2 and 10 m/sec, the ‘V’ and ‘X’ crush modes [Ruan, Lu, Wang and Yu (2003)] appears near both the moving and fixed ends. For the cases under higher velocities, 50 and 100 m/sec, the cells near moving end are progressively collapsed and highly condensed, which also form a front of crush similar to the shock front in wave propagation [Zou, Reid, Tan, Li, and Harrigan (2009)]. The

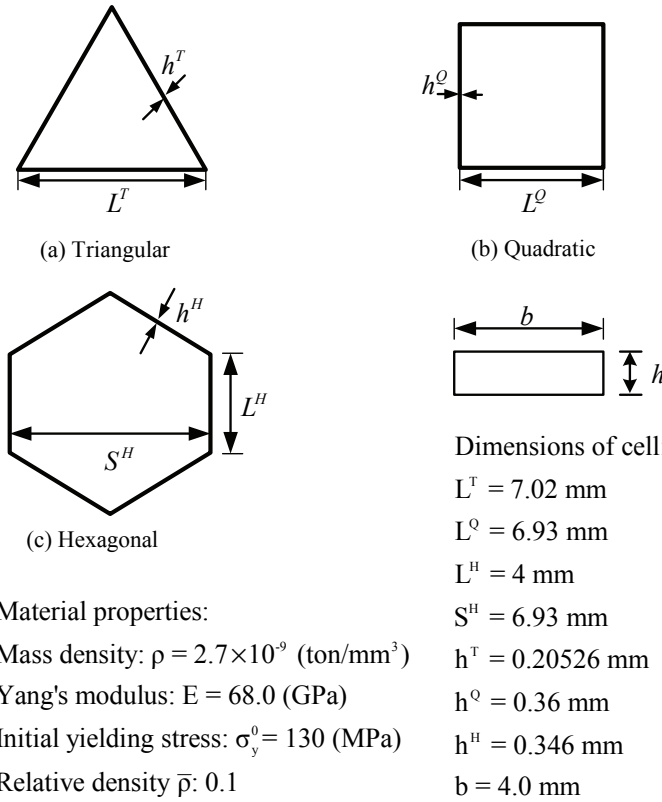


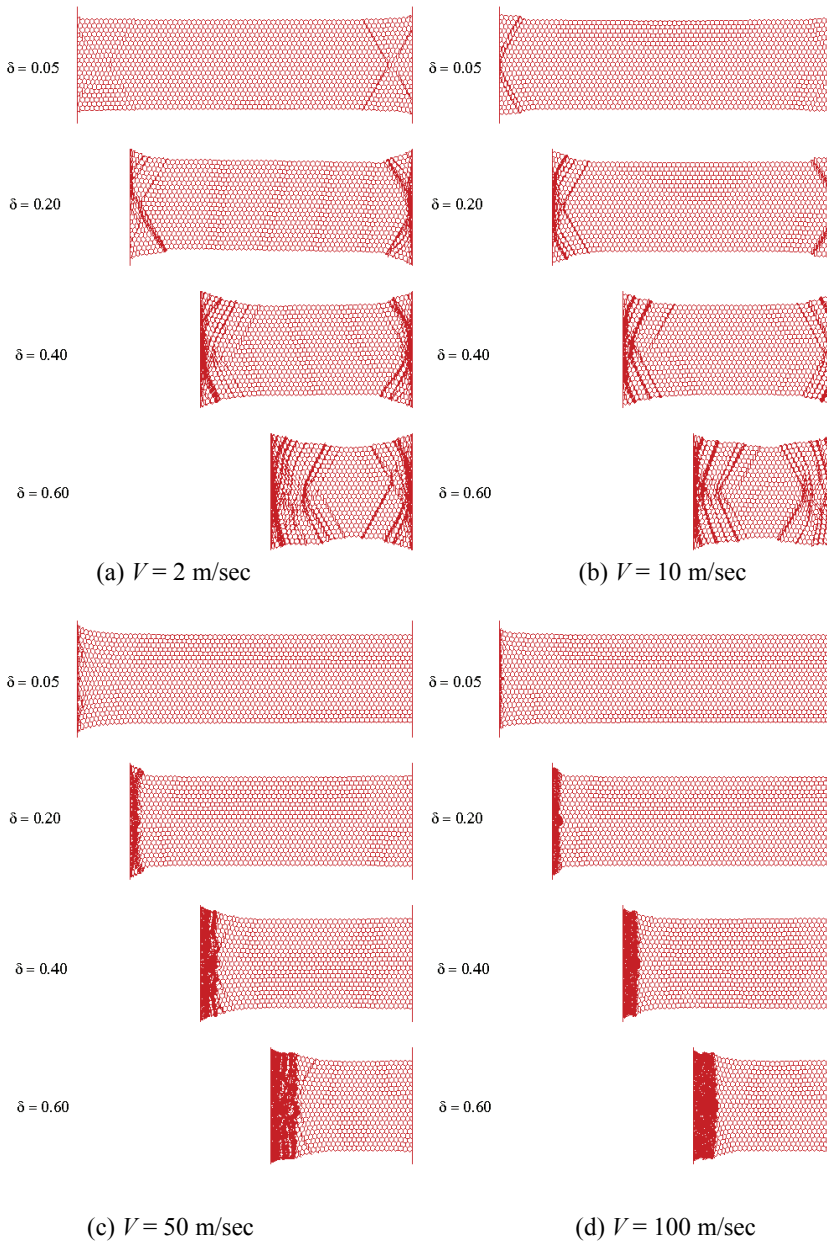
Figure 16: Dimensions and material properties of each single cell in **Figure 15**.

same analyses had been conducted by Zou, Reid, Tan, Li, and Harrigan (2009) using commercial code and comparing their results with 2 one-dimensional shock theories. The first one can be found in the references by Reid and Peng, (1997); Tan, Reid, Harrigan, Zou, and Li (2005); Tan, Harrigan, and Reid (2002),

$$\sigma = \sigma_0 + \frac{\rho V^2}{\epsilon_d} \tag{51}$$

where, σ_0 and σ denote the quasi-static and dynamic plateau stress, ρ the initial density of the cellular material ϵ_d the densification strain. The second one further incorporates the Rankine-Hugoniot jump conditions,

$$\sigma = \sigma_A + \frac{\rho [V]^2}{[\epsilon]} \tag{52}$$

Figure 17: Deformation process of *Type I* cellular material

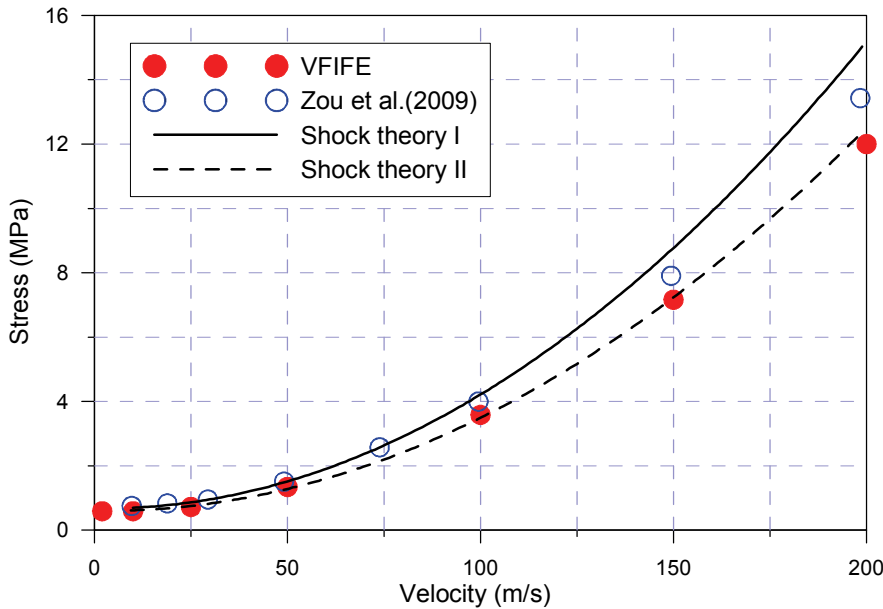


Figure 18: Plateau stress vs. compression velocity of *Type I* cellular material.

where σ_A and is the stress just ahead of the shock and [] denotes a change in the value across the shock [Harrigan, Reid, Tan and Reddy (2005)].

Figure 18 plots the plateau stress versus compression velocity of *Type I* cellular material. It can be found that the result of VFIFE is more close to theory considering the Rankine-Hugoniot jump conditions.

Figure 19 and **20** respectively plots the deformation process of *Type II* and *III* materials under compression velocities, 2, 10, 50, and 100 m/sec. In these results, only the ‘I’ crush mode appears under each compression velocity. For the case of *Type II*, largely vertical dislocations due to the shear instability on cell walls therein are found, when compression velocities are 2 and 10 m/sec. Under the velocities of 50, and 100 m/sec, the dislocations disappear but some cells are distorted before crushing (see **Figure 19**). For the case of *Type III*, the deformation process is smoother than the other two.

Figure 21 shows the plateau stresses versus compression velocity of the three materials, in which the curves fitted by quadratic polynomial function are also plotted. It can be observed that the *Type III* has higher plateau stress as compression velocity is slower than around 40 m/sec. As the compression velocity is greater than 40 m/sec, the plateau stress of *Type II* and *III* are almost the same, but significantly

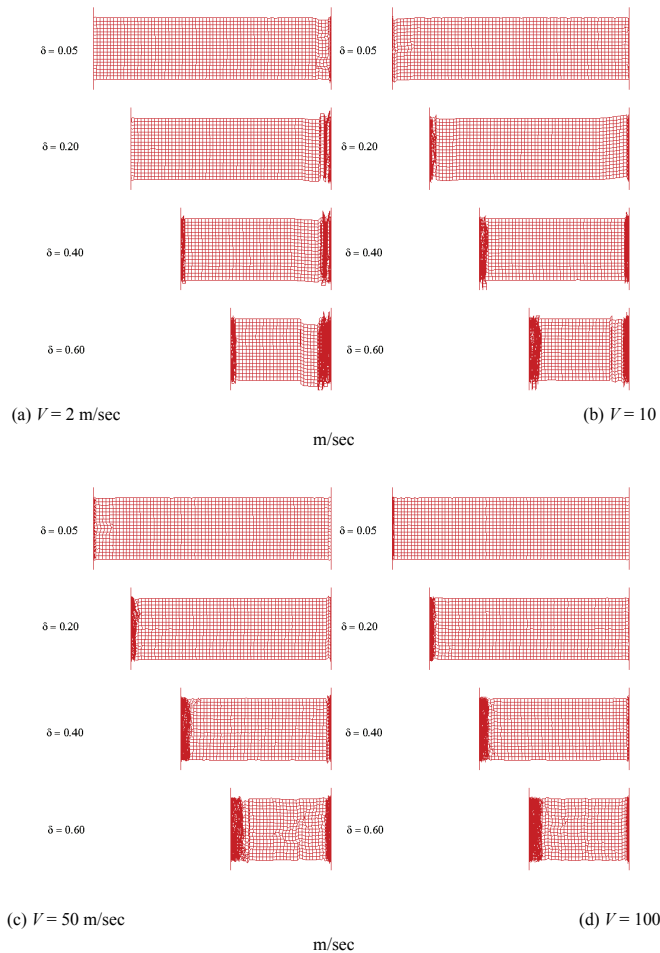


Figure 19: Deformation process of *Type II* material.

smaller than that of *Type I*.

5.3 Example 3: Crushing of honeycombs with stiff inclusions

In this example, crushing behaviors of honeycombs with stiff inclusions are examined. **Figure 22** illustrates a honeycomb consisting of 20×21 single cells, which is installed between 2 plates, A and B. The geometric and material properties are also illustrated and specified in **Figure 22**. The plate A is driven by a constant velocity 1 m/s to compress the honeycomb. In order to explore the influence of stiff inclusions on the honeycomb, 2 and 6 lines of inclusions are respectively arranged

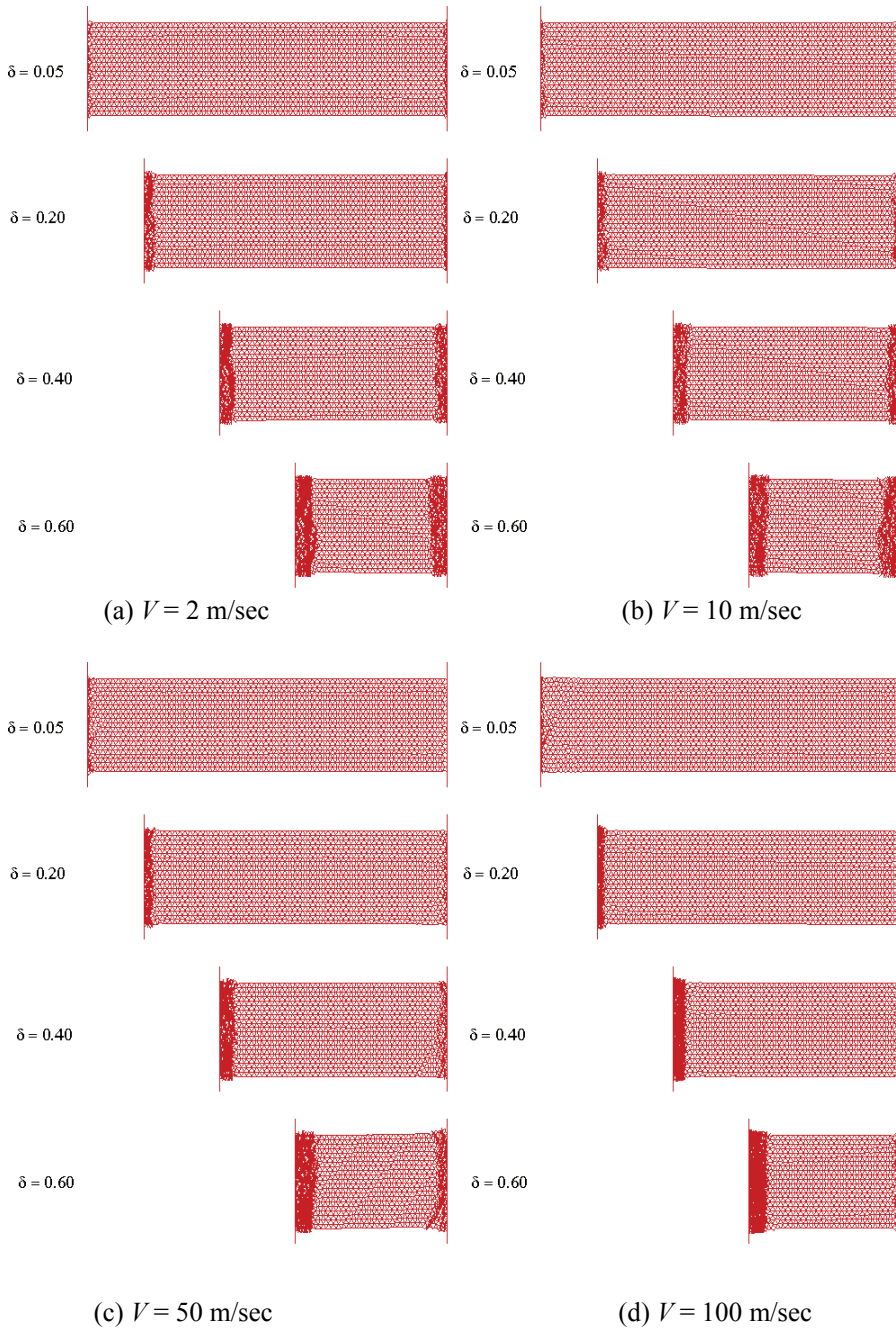


Figure 20: Deformation process of *Type III* material.

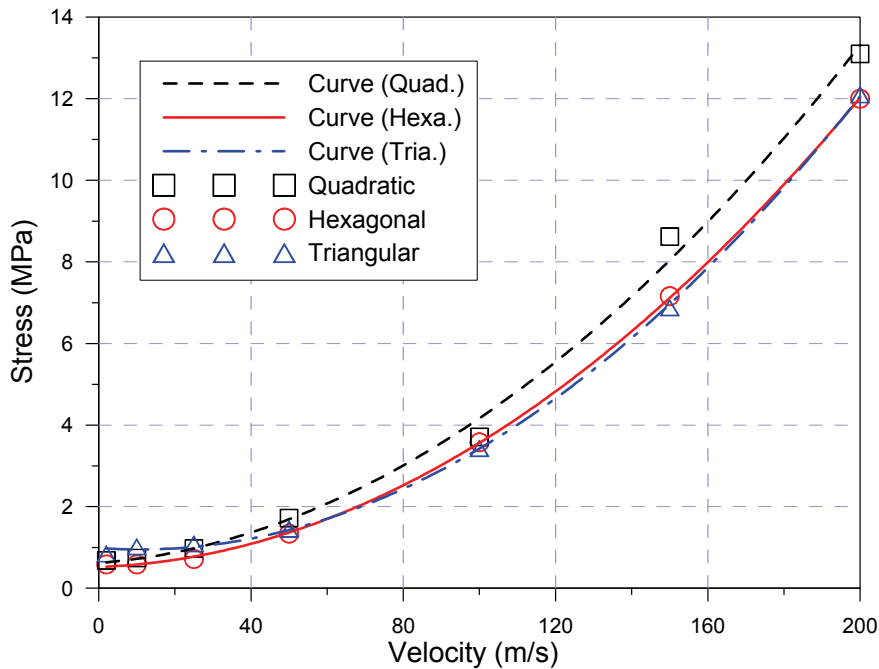
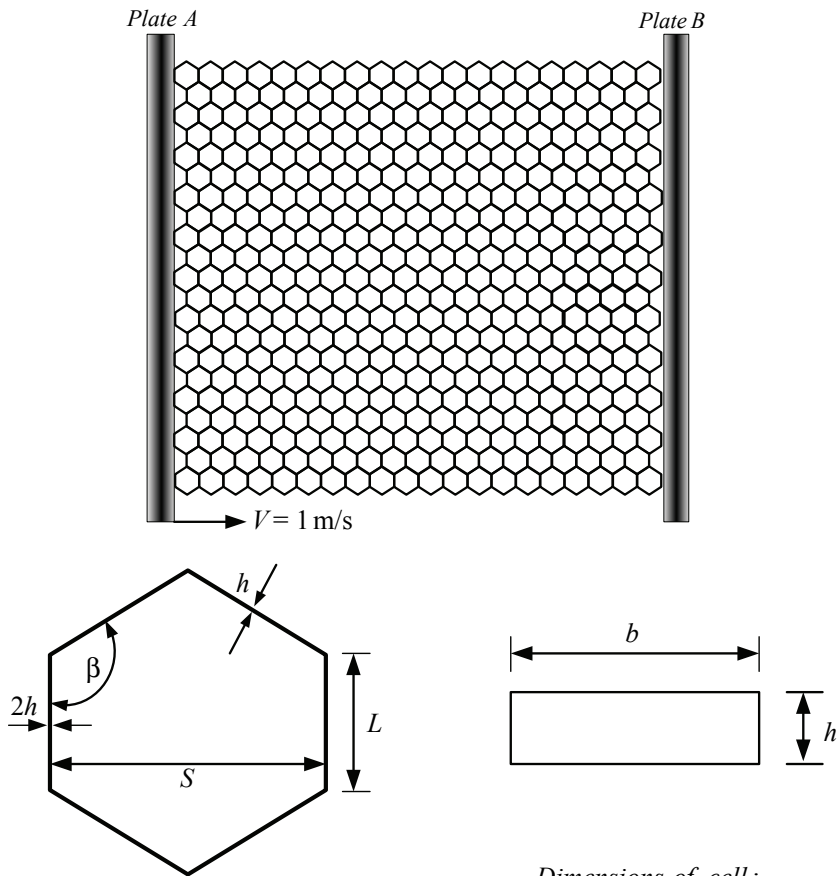


Figure 21: Plateau stresses vs. compression velocity of the three types of materials.

into the honeycomb illustrated in **Figure 22**, as shown in **Figure 23**. In analysis, a single cell wall is modeled by 11 particles and 10 beam elements. 2 and 6 integration points are respectively allocated along the axis and through section depth of the beam element to evaluate internal forces. The inclusions are modeled via using relative stiff elements. In addition, a size of time step $\Delta t = 2 \times 10^{-8}$ sec is used for time integration.

Figure 24 and **Figure 25** plot the stress-displacement curves of the two honeycombs with inclusions and compared with that without inclusion. It is found the stiff inclusions significantly affect the densification displacement (strain) and compression stress. The densification displacements are around 120 mm for the honeycomb without inclusion, around 100 mm for that with 2 lines of inclusions, and around 85 mm for that with 6 lines of inclusions. Furthermore, 2 and 6 salient peaks before densification can be observed in **Figure 24** and **Figure 25** respectively. They are consistent with the number of lines of inclusions. In fact, Nakamoto, Adachi, and Araki (2009) had conducted this example using commercial code. In their results, 2 salient peaks appear in the curve of the case with 2 lines of inclusions. However, none of salient peaks in the case with 6 lines of inclusions are found.



Material properties :

Mass density: $\rho = 2.7 \times 10^{-9} \text{ (ton/mm}^3\text{)}$

Poisson ratio: $\nu = 0.33$

Yang's modulus: $E = 70.0 \text{ (GPa)}$

Initial yielding stress: $\sigma_y^0 = 34 \text{ (MPa)}$

Dimensions of cell :

$S = 8.66 \text{ mm}$

$L = 5.0 \text{ mm}$

$\beta = 120^\circ$

$h = 0.1 \text{ mm}$

$b = 5.0 \text{ mm}$

Figure 22: The honeycomb without stiff inclusions and the properties of a single cell.

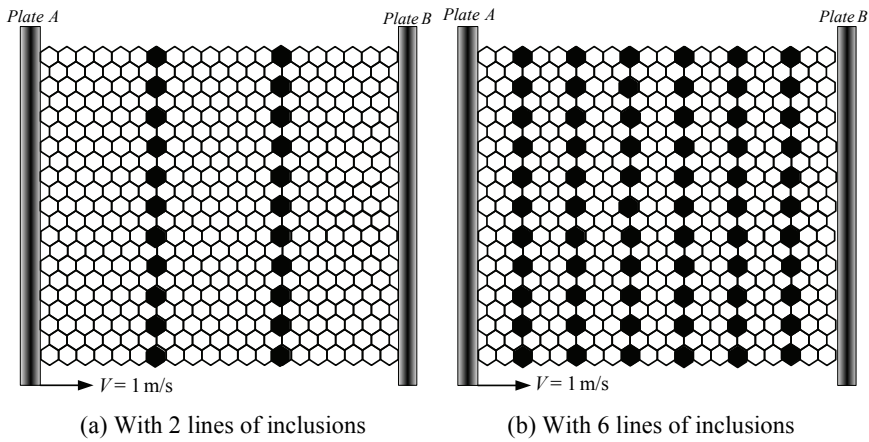


Figure 23: The honeycombs inserted (a) 2 lines and (b) 6 lines of inclusions.

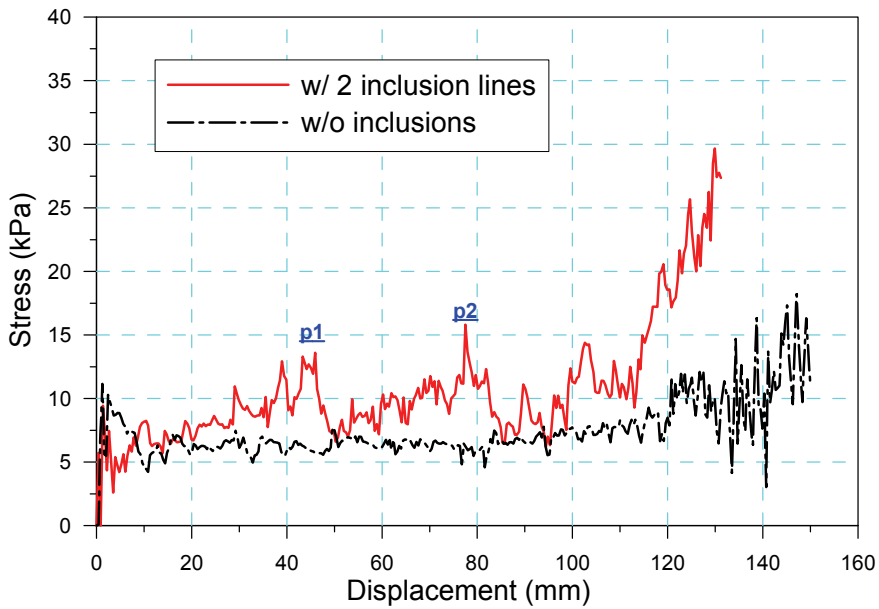


Figure 24: The stress vs. displacement curves (w/o and w/ 2 lines of inclusions).

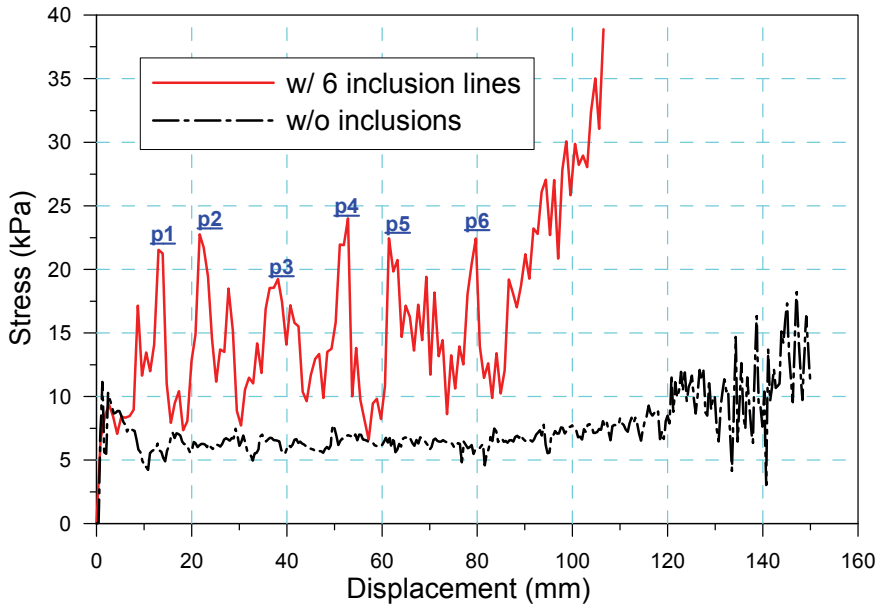


Figure 25: The stress vs. displacement curves (w/o and w/ 6 lines of inclusions).

Figure 26 shows the deformation process of the honeycomb without inclusions. An X-mode of crushing appears when the compression displacement is around 40 mm. This is a common phenomenon in honeycomb compression test [Papka and Kyriakides (1998)]. **Figure 27** shows the deformation process of the honeycomb with 2 lines of inclusions. Firstly, a V-mode of crushing arises as the plate displacement is around 21 mm. Then it is turned into C-mode due to hitting the first line of inclusions as the plate displacement is around 40.3 mm. The crushing mode of the cells locating between the 2 lines of inclusions is in the form of I-mode. **Figure 28** shows the deformation process of the honeycomb with 6 lines of inclusions. Only I-mode of crushing is found in each phase of compression.

6 Conclusions

In this paper, an analysis framework centered at VFIFE to simulate crushing of cellular materials has been established. The method of VFIFE is developed based on vector mechanics. It is suitable to solve the problems with multiple nonlinearities. Its algorithm does not involve any matrix operation. In the proposed framework the memory requisition and CPU cost can be controlled in linear range via incorporating the NBS contact detection approach. Thus the algorithm is very suitable for

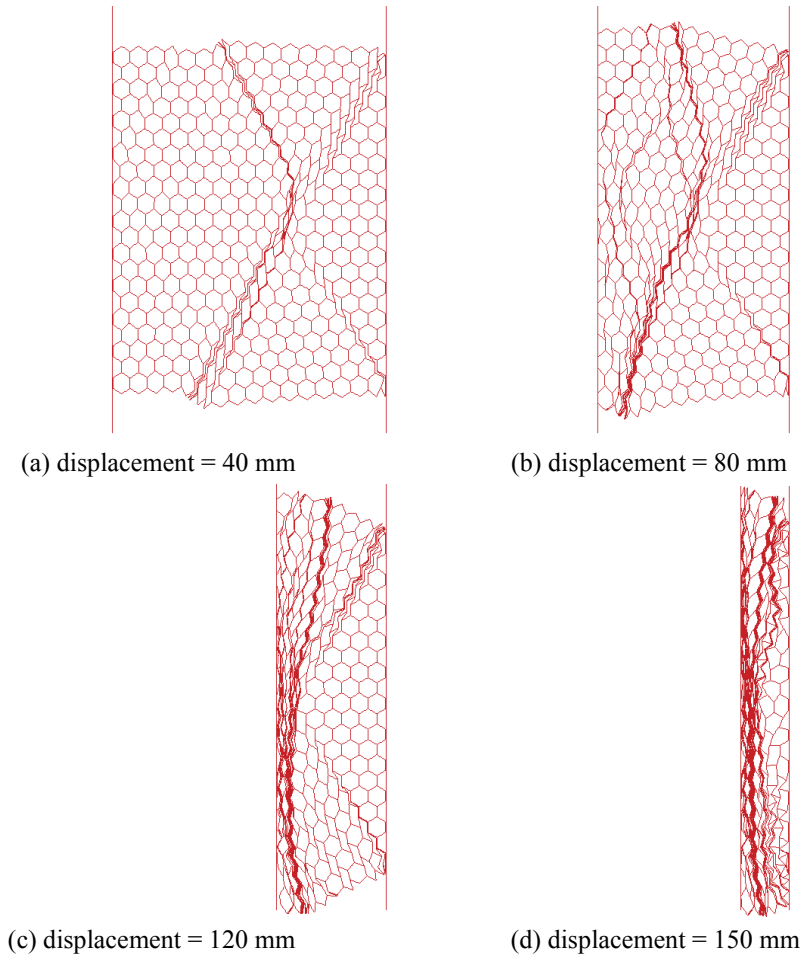


Figure 26: The deformation process of the honeycomb without inclusions.

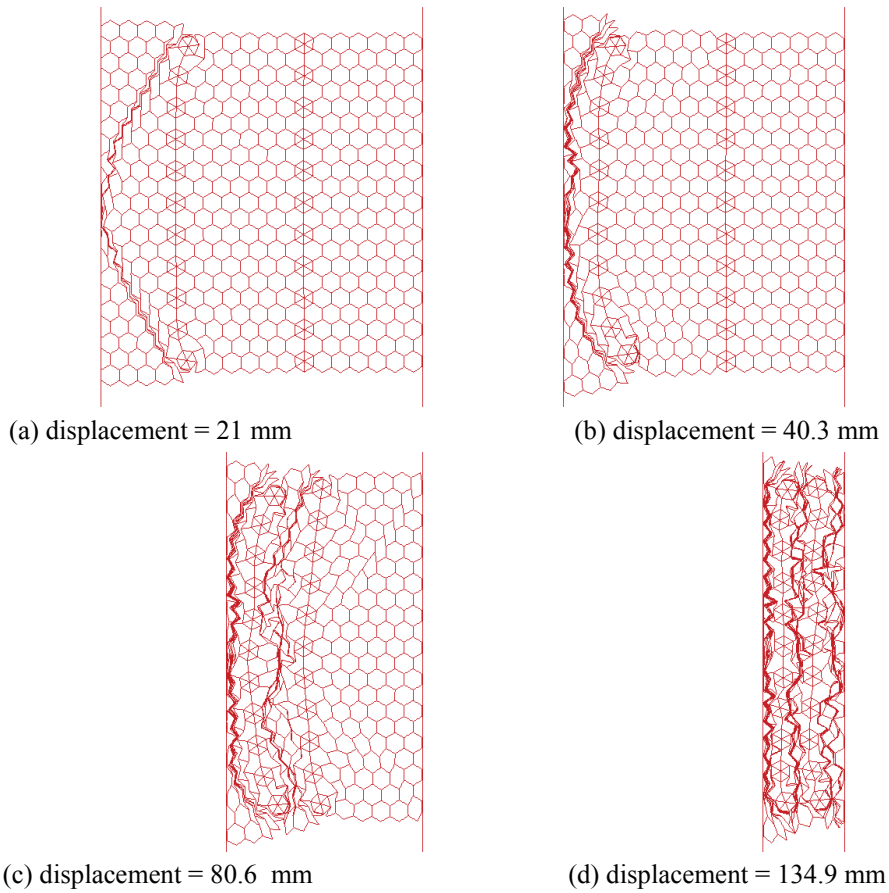


Figure 27: The deformation process of the honeycomb with 2 lines of inclusions.

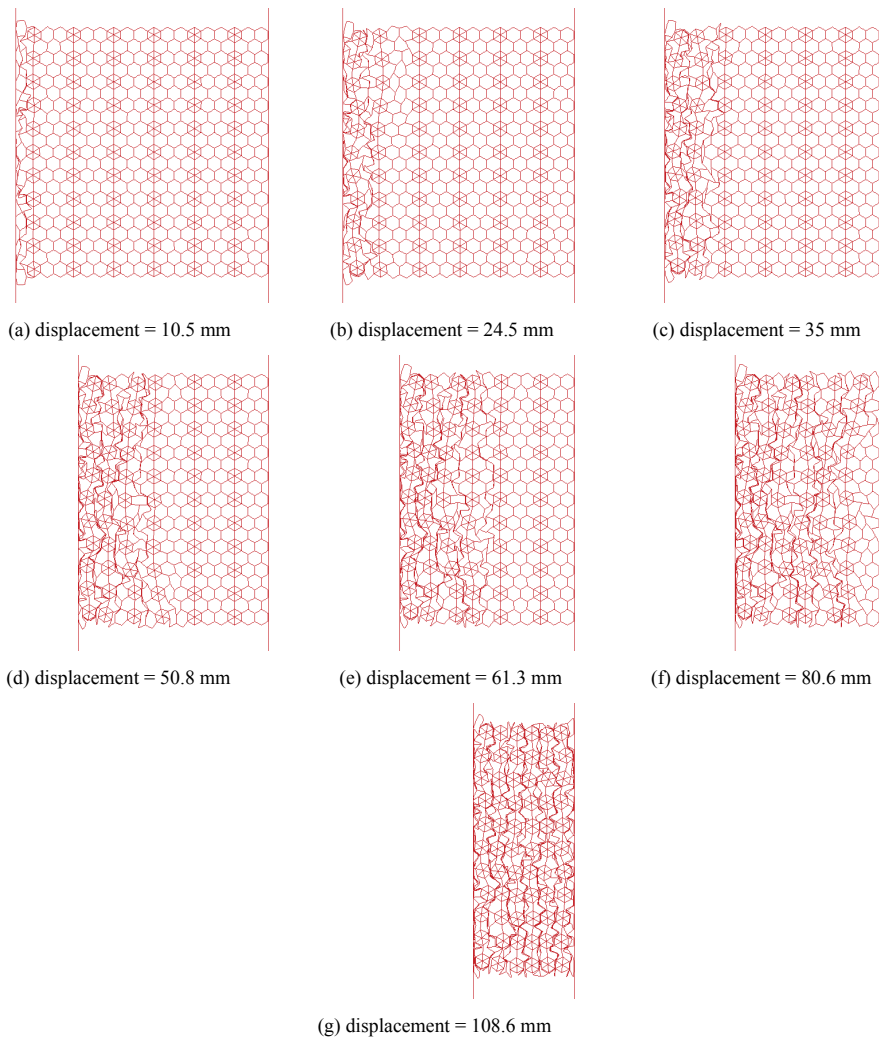


Figure 28: The deformation process of the honeycomb with 6 lines of inclusions.

parallel computing to treat large scale simulations, which will be explored and presented in the subsequently published papers. Numerical results performed reveals that the procedures proposed in this paper are sound and reliable to simulate failure and crushing of diverse cellular materials.

References:

Cai, Y. C.; Paik, J. K.; Atluri, S. N. (2010): Locking-free thick-thin rod/beam element for large deformation analyses of space-frame structures based on the Reissner variational principle and a von Karman type nonlinear theory. *CMES: Computer Modeling in Engineering & Sciences*, vol.58, pp.75-108.

Cai, Y.C.; Paik, J.K.; Atluri, S.N. (2009a): Large deformation analyses of space frame structures, with members of arbitrary cross-section, using explicit tangent stiffness matrices, based on a von Karman type nonlinear theory in rotated reference frames. *CMES: Computer Modeling in Engineering & Sciences*, vol. 53, pp.123-152.

Cai, Y.C.; Paik, J.K.; Atluri, S.N. (2009b): Large deformation analyses of space frame structures, using explicit tangent stiffness matrices, based on the Reissner variational principle and a von Karman type nonlinear theory in rotated reference frames. *CMES: Computer Modeling in Engineering & Sciences*, vol. 54, pp.335-368.

Gibson, L. J.; Ashby, M. F. (1997): *Cellular solids: structure and properties* (2nd ed). Cambridge: Cambridge University Press, pp. 93-147.

Gibson, L. J.; Ashby, M. F.; Schajer, G. S.; Robertson, C.I. (1982): The mechanics of two-dimensional cellular materials. *Proc. R. Soc. London*, vol. 382, pp. 25-42.

Gibson, L. J.; Ashby, M. F. (1982): The mechanics of three-dimensional cellular materials. *Proc. R. Soc. London*, vol. 382, pp. 43-59.

Guo, X. E.; Gibson, L. J. (1997): Behavior of intact and damaged honeycombs: a finite element study. *Int. J. Mech. Sci.*, vol. 41, pp. 85-105.

Harrigan, J. J.; Reid, S. R.; Tan, P. J.; Reddy, T. Y. (2005): High rate crushing of wood along the grain. *Int. J. Solids Struct.*, vol. 47, pp. 521-44.

Hönig, A.; Stronge, W. J. (2002a): In-plane dynamic crushing of honeycomb. Part I: crush band initiation and wave trapping. *Int. J. Mech. Sci.*, vol. 44, pp. 1665-1696.

Hönig, A.; Stronge, W. J. (2002b): In-plane dynamic crushing of honeycomb. Part II: application to impact. *Int. J. Mech. Sci.*, vol. 44, pp. 1697-1714.

Iura, M.; Suetake, Y.; Atluri, S.N. (2003): Accuracy of Co-rotational Formula-

tion for 3-D Timoshenko's Beam, *CMES: Computer Modeling in Engineering & Sciences*, Vol.4, No.2, pp. 249-258.

Krieg, R. D.; Key, S. W. (1976): Implementation of a time dependent plasticity theory into structural computer programs. *Constitutive Equations in Viscoplasticity: Computational and Engineering Aspects*, ASME, vol. 20, pp. 125-137.

Li, K.; Gao, X. L.; Wang, J. (2007): Dynamic crushing behavior of honeycomb structures with irregular cell shapes and non-uniform cell wall thickness. *Int. J. Solids Struct.*, vol. 44, pp. 5003–5026.

Liu, Y.; Zhang, X. C. (2009): The influence of cell micro-topology on the in-plane dynamic crushing of honeycombs. *Int. J. Impact Eng.*, vol. 36, pp. 98-109.

Munjiza A.; Andrews, K. R. F. (1998): NBS contact detection algorithm for bodies of similar size. *Int. J. Numer. Meth. Engng.*, vol. 66, pp. 46-71

Nakamoto H.; Adachi T.; Araki W. (2009a): In-plane impact behavior of honeycomb structures randomly filled with inclusions. *Int. J. Impact Eng.*, vol. 36, pp. 73-80.

Nakamoto H.; Adachi T.; Araki W. (2009b): In-plane impact behavior of honeycomb structures filled with linearly arranged inclusions. *Int. J. Impact Eng.*, vol. 36, pp. 1019-1026.

Papka, S. D.; Kyriakides S. (1994): In-plane compressive response and crushing of honeycomb. *J. Mech. Phys. Solids*, vol. 42, pp. 1499–532.

Papka, S. D.; Kyriakides, S. (1998): Experiments and full scale numerical simulations of in-plane crushing of a honeycomb. *Acta. Mater.*, vol. 46, pp. 2765-2776.

Reid, S. R.; Reddy, T. Y.; Peng, C. (1993): Dynamic compression of cellular structures and materials. *Structural Crashworthiness and Failure* (Ed. by Jones N and Wierzbicki T). London: Elsevier Applied Science Publishers, pp. 295-340.

Reid, S. R.; Peng, C. (1997): Dynamic uniaxial crushing of wood. *Int. J. Impact Eng.*, vol. 19, pp. 531-570.

Ruan, D.; Lu, G.; Wang, B.; Yu, T. X. (2003): In-plane dynamic crushing of honeycombs –a finite element study. *Int. J. Impact Eng.*, vol. 28, pp. 161-182.

Silva, M. J.; Gibson L. J. (1997): The effect of non-period microstructure and defects on the compressive strength of two-dimensional cellular solids. *Int. J. Mech. Sci.*, vol. 39, pp. 549-563.

Shi, C.; Wang, Y. K.; Ting, E. C. (2004): Fundamentals of a Vector Form Intrinsic Finite Element: Part III Convected Material Frame and Examples. *J. Mech.*, vol. 20, pp. 133-143.

Tan, P. J.; Reid, S. R.; Harrigan, J. J.; Zou, Z.; Li, S. (2005): Dynamic compres-

sive strength properties of aluminum foams. Part II-shock theory and comparison with experimental data and numerical models. *J. Mech. Phys. Solids*, vol. 53, pp. 2206-2230.

Tan, P. J.; Harrigan, J. J.; Reid, S. R. (2002): Inertia effects in uniaxial dynamic compression of a closed cell aluminum alloy foam. *Mater. Sci. Technol.*, vol. 18, pp. 480-488.

Ting, E. C.; Shi C.; Wang Y. K. (2004a): Fundamentals of a vector form intrinsic finite element: Part II Plane solid element. *J. Mech.*, vol. 20, pp. 123-132.

Ting, E. C.; Shi C.; Wang, Y. K. (2004b): Fundamentals of a vector form intrinsic finite element: Part I Basic procedure and a planar frame element. *J. Mech.*, vol. 20, pp. 113-122.

Ting, E. C.; Wang, C. Y.; Wu, T. Y.; Wang, R. Z.; Chuang, C. C. (2006): *Motion analysis and vector form intrinsic finite element*. Report No. CBER-2006-W-001, V-5 Research Group, National Central University, Taiwan, (in Chinese).

Wu, T. Y.; Wang, R. Z.; Wang, C. Y. (2006): Large deflection and transient analysis of planar flexible frames. *J. Chinese Inst. Eng.*, vol. 29, pp. 593-606.

Wu, T. Y.; Ting E. C. (2004): Vector form intrinsic finite element for 3D solids. *Proceedings of the 28th National Conference on Theoretical and Applied Mechanics*, Taipei (in Chinese).

Wu, T. Y.; Wang, C. Y.; Chuang, C. C.; Ting, E. C. (2007): Motion analysis of 3D membrane structures by a vector form intrinsic finite element. *J. Chinese Inst. Eng.*, vol. 30, pp. 961-976,

Wu, T. Y.; Ting, E. C. (2008): Large deflection analysis of 3D membrane structures by a 4-node quadrilateral intrinsic element, *Thin-Walled Struct.*, vol. 46, no. 3, pp. 261-275.

Wu, T. Y.; Lee, J. J.; Ting, E. C. (2008): Motion analysis of structures (MAS) for flexible multibody system: planar motion of solids, *Multibody Syst. Dyn.*, vol. 20, no. 3, pp. 197-221.

Wu, T. Y.; Tsai, W. C.; Lee, J. J. (2009): Dynamic elastic-plastic and large deflection analyses of frame structures using motion analysis of structures, *Thin-Walled Struct.*, vol. 47, pp. 1177-1190.

Zheng, Z.; Yu, J.; Li, J. (2005): Dynamic crushing of 2D cellular structures: a finite element study. *Int. J. Impact Eng.*, vol. 32, pp. 650-664.

Zhong, Z. H. (1993): *Finite element procedures for contact-impact problems*. Oxford University Press.

Zou, Z.; Reid, S. R.; Tan, P. J.; Li, S.; Harrigan, J. J. (2009): Dynamic crushing of honeycombs and features of shock front. *Int. J. Impact Eng.*, vol. 36, pp. 165-

176.

Zhu, H. H.; Cai, Y. C.; Paik, J. K.; Atluri, S. N. (2010): Locking-free thick-thin rod/beam element based on a von Karman type nonlinear theory in rotated reference frames for large deformation analyses of space-frame structures. *CMES: Computer Modeling in Engineering & Sciences*, vol.57, pp.175-204.